5-2017

On the Simulation and Mitigation of Anisoplanatic Optical Turbulence for Long Range Imaging

Russell C. Hardie
University of Dayton, rhardie1@udayton.edu

Daniel A. LeMaster
Air Force Research Laboratory

On the simulation and mitigation of anisoplanatic optical turbulence for long range imaging

Russell C. Hardie[a] and Daniel A. LeMaster[b]

[a]University of Dayton, Department of Electrical and Computer Engineering, 300 College Park, Dayton OH, USA, 45459-0232

[b]Air Force Research Laboratory, AFRL/RYMT, Building 620, 2241 Avionics Circle, Wright-Patterson AFB, Ohio, USA, 45433

ABSTRACT

We describe a numerical wave propagation method for simulating long range imaging of an extended scene under anisoplanatic conditions. Our approach computes an array of point spread functions (PSFs) for a 2D grid on the object plane. The PSFs are then used in a spatially varying weighted sum operation, with an ideal image, to produce a simulated image with realistic optical turbulence degradation. To validate the simulation we compare simulated outputs with the theoretical anisoplanatic tilt correlation and differential tilt variance. This is in addition to comparing the long- and short-exposure PSFs, and isoplanatic angle. Our validation analysis shows an excellent match between the simulation statistics and the theoretical predictions. The simulation tool is also used here to quantitatively evaluate a recently proposed block-matching and Wiener filtering (BMWF) method for turbulence mitigation. In this method block-matching registration algorithm is used to provide geometric correction for each of the individual input frames. The registered frames are then averaged and processed with a Wiener filter for restoration. A novel aspect of the proposed BMWF method is that the PSF model used for restoration takes into account the level of geometric correction achieved during image registration. This way, the Wiener filter is able fully exploit the reduced blurring achieved by registration. The BMWF method is relatively simple computationally, and yet, has excellent performance in comparison to state-of-the-art benchmark methods.

Keywords: atmospheric turbulence, anisoplanatic, simulation, optical wave propagation, tubulence mitigation

1. INTRODUCTION

Long range imaging in the atmosphere is often limited, by optical turbulence.[1] Under anisoplanatic imaging conditions, this turbulence causes spatially and temporally varying warping and blurring. We have developed a new numerical wave propagation tool to simulate anisoplanatic optical turbulence.[2] We present some of the key aspects of this simulation tool here along with a validation analysis. Furthermore, we use this simulation tool to quantitatively evaluate a recently proposed block matching and Wiener filtering (BMWF) method, developed in part by one of current authors.[3] This paper serves to summarize key aspects of the author's simulation tool[2]

Long-Range Imaging II, edited by Eric J. Kelmelis, Proc. of SPIE Vol. 10204, 102040B · © 2017 SPIE · CCC code: 0277-786X/17/$18 · doi: 10.1117/12.2264064

and the BMWF method.[3] Some sections include condensed content from the authors previous papers.[2,3] New data is used in the simulation results.

Our simulation method is based on that of Bos and Roggemann.[4] Other related methods can be found in.[5–9] We use numerical wave propagation starting from a grid of point sources in the object plane. The propagation passes through a series of extended phase screens. This results in an array of spatially correlated point spread functions (PSFs). The PSFs are then used in a spatially varying weighted sum operation with an ideal image to produce a simulated image with realistic optical turbulence degradation. Noise and other degradations can be incorporated as well. With our method we are able to simulate constant and varying $C_n^2(z)$ profiles. Furthermore, we are able to simulate sequences with both temporally independent and temporally correlated turbulence effects. Temporal correlation is introduced by generating larger extended phase screens, and translating this block of screens in front of the propagation area. This approach is similar to that described by Dios *et al.*[10]

The ability to accurately simulate the optical turbulence is important because it allows us to quantitatively evaluate turbulence mitigation methods.[3,5,11,12] With the simulation, an objective truth image is available. When such truth is not available, assessment of restoration algorithms is limited to subjective and sometimes unreliable methods. Thus, a critical step in advancing turbulence mitigation algorithms is to develop accurate degradation simulation tools.

To validate our simulation, we use metrics that related to both geometric warping and blurring. To evaluate the warping component of the model, we use the theoretical anisoplanatic tilt correlation[13] and and a derived differential tilt variance statistic.[2] To validate the blurring in the simulation, we examine the long-exposure and average short-exposure PSFs. Our validation analysis shows an excellent match between the simulation statistics and the theoretical predictions.

In this paper, we also summarize the block-matching and Wiener filtering (BMWF) turbulence mitigation method proposed in.[3] With this method, input frames are globally registered and averaged to form a prototype image with the approximately correct geometry. A block matching algorithm (BMA) is used to warp the individual input frames to match the prototype. The BMA registered frames are then averaged to generate a fused image. The final step is deconvolving the fused image using a Wiener filter. An important novel aspect of the proposed method lies in how we model the degradation PSF. We use a parametric model that takes into account the level of geometric correction achieved during image registration. By matching the PSF to the level of registration in this way, the Wiener filter is able fully exploit the reduced blurring achieved by registration. Our experimental results include the use of both simulated and real imagery.

The rest of the paper is organized as follows. The simulation tool is described in Section 2. The BMWF method is presented in Section 3. The experimental results are presented in Section 4. These include some simulation validation results and BMWF turbulence mitigation results. Finally, we offer conclusions in Section 5.

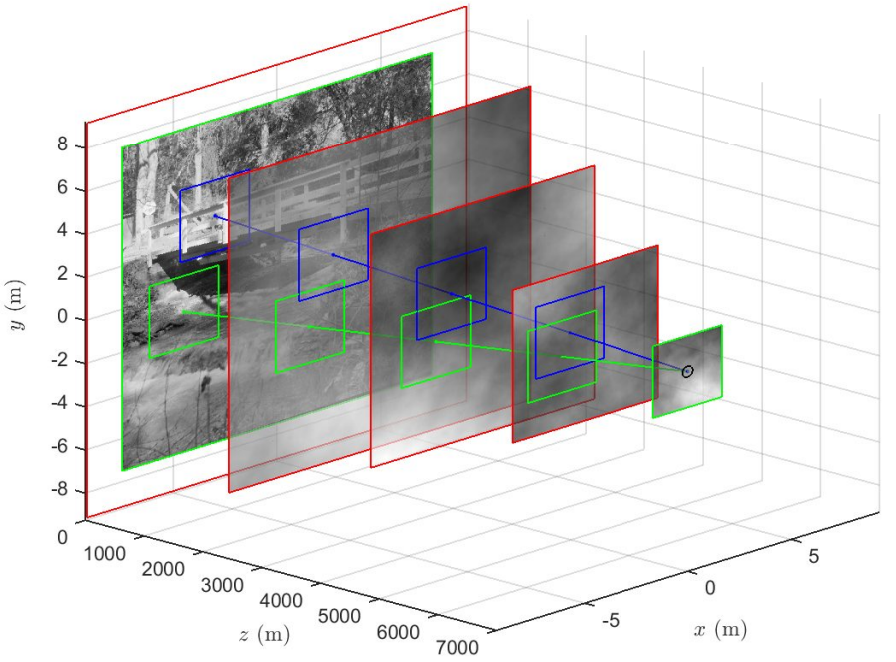

Figure 1. Phase screen geometry for anisoplanatic PSF array generation.

2. ANISOPLANATIC OPTICAL TURBULENCE SIMULATION

2.1 Simulation geometry

As mentioned in Section 1, the proposed method is based on the method of Bos and Roggemann.[4] Extended phase screens are generated as shown in Fig. 1. Points in the object plane are projected to the center of the camera pupil. Two such examples are shown in Fig. 1. The local phase screens are cropped from the extended phase screens within a specified distance of the optical path for each point. These local phase screen portions are shown with the blue and green squares in Fig. 1. The extended phase screen sizes are determined based on the cropped phase screen size and the object size, as shown in Fig. 1.

2.2 Numerical wave propagation

A simulated point source is numerically propagated from the object plane to the pupil plane though the cropped phase screens for each point in the object plane. The grid of object points is spaced according to the Nyquist sample spacing in the object plane. A split-step propagation method[14] is applied to each of the point sources. This propagates the wavefunction through the phase screens and to the pupil plane. The split-step method used to form each PSF is illustrated in Fig. 2.

2.3 PSF and image generation

Following the propagations, the complex amplitude at the pupil plane, $u_N(x, y)$, is obtained. This is multiplied by the camera aperture mask, $a(x, y)$, and a collimation-type phase compen-

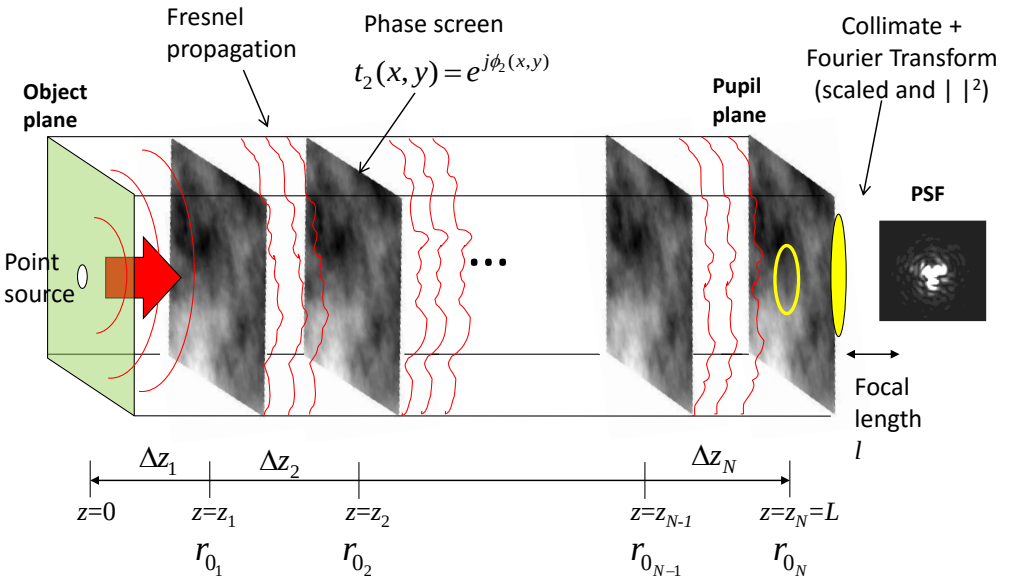

Figure 2. Illustration of the split-step propagation used to generate each individual PSF. The local phase screens shown are cropped from larger screens based on the point source location in the object plane, as shown in Fig. 1.

sation is used to allow the lens operation to focus the image at the focal length. This yields,

$$p(x,y) = a(x,y)u_N(x,y)\exp\left(\frac{-j\pi(x^2+y^2)}{\lambda L}\right), \tag{1}$$

where L is the full propagation path length. The incoherent PSF can be found based on Eq. (1), and is given by[15]

$$h(x,y) = \left(|P(u,v)|^2\right)\Big|_{u=\frac{x}{\lambda l}, v=\frac{y}{\lambda l}}, \tag{2}$$

where $P(u,v) = FT\{p(x,y)\}$ and $FT\{\cdot\}$ is the Fourier transform, and λ is the wavelength, and l is the focal length of the camera optics. In practice, the PSF is evaluated discretely using the FFT and then resampled to the focal plane Nyquist spacing for the camera. We also normalize the discrete PSFs to all have a sum of 1.[4] The final simulation output is computed with a spatially varying weighted sum as

$$z(m,n) = \sum_k \sum_l o(m-k, n-l)h_{m,n}(k,l), \tag{3}$$

where $o(m,n)$ is the ideal discrete object image, and $h_{m,n}(k,l)$ is the Nyquist sampled discrete PSF associated with object sample (m,n).

2.4 Phase Screens

Phase screen realizations are designed to follow a modified von Kármán phase power spectral density (PSD).[14] This PSD includes the Kolmogorov PSD as a special case, but has additional

parametric flexibility. The modified von Kármán PSD is given by

$$S_{\phi_i}{}^{mvK}(\rho) = \frac{0.023\mathrm{e}^{-\rho^2/\rho_m^2}}{r_{0_i}^{5/3}(\rho^2+\rho_0^2)^{11/6}}, \tag{4}$$

where $\rho = \sqrt{u^2+v^2}$, $\rho_m = 5.92/(2\pi l_0)$, and $\rho_0 = 1/L_0$. Note that the radial spatial frequency, ρ, is measured in units of cycles/meter, and r_{0_i} is the i'th phase screen Fried parameter. The parameters l_0 and L_0 are the inner and outer turbulence scales, respectively.[14] Note that for $l_0 = 0$ and $L_0 = \infty$, the modified von Kármán PSD is equivalent to a Kolmogorov PSD.[14]

The individual phase screen Fried parameters are determined such that they are consistent with the global Fried parameter, log-amplitude variance, and isoplanatic angle. This approach is based on the method presented by Schmidt,[14] but we have extended this to also include the isoplanatic angle.[2]

3. TURBULENCE MITIGATION

3.1 Optical transfer functions

When imaging in atmospheric turbulence, the overall camera optical transfer function (OTF) can be modeled to include the atmospheric OTF and the diffraction OTF. This is given by

$$H_\alpha(\rho) = H_{\mathrm{atm},\alpha}(\rho)H_{\mathrm{dif}}(\rho). \tag{5}$$

The atmospheric OTF model typically used is given by[16]

$$H_{\mathrm{atm},\alpha}(\rho) = \exp\left\{-3.44\left(\frac{\lambda l\rho}{r_0}\right)^{5/3}\left[1-\alpha\left(\frac{\lambda l\rho}{D}\right)^{1/3}\right]\right\}. \tag{6}$$

The parameter r_0 is the Fried parameter, and D is the aperture diameter of the camera optics. The parameter α (or $\beta = \sqrt{1-\alpha}$) relates to the level of motion blur from tilt variance. When $\alpha = 0$ ($\beta = 1$), we get the long exposure OTF model. When $\alpha = 1$ ($\beta = 0$), we get the average short exposure OTF. The diffraction-limited OTF for a circular exit pupil is given by[15]

$$H_{\mathrm{dif}}(\rho) = \begin{cases} \frac{2}{\pi}\left[\cos^{-1}\left(\frac{\rho}{2\rho_c}\right) - \frac{\rho}{2\rho_c}\sqrt{1-\left(\frac{\rho}{2\rho_c}\right)^2}\right] & \rho \le \rho_c \\ 0 & \text{otherwise} \end{cases}, \tag{7}$$

where $\rho_c = 1/(\lambda f/\#)$ is the optical cut-off frequency, and the f-number is $f/\# = l/D$.

The authors have proposed tuning the parameter α to the level of tilt correction in any registration step used in turbulence mitigation.[3] For ideal registration, $\alpha = 1$ would be used. When no registration is employed, we use $\alpha = 0$. This is in contrast to conventional methods that often assume $\alpha = 0$, regardless of any registration steps employed.[3]

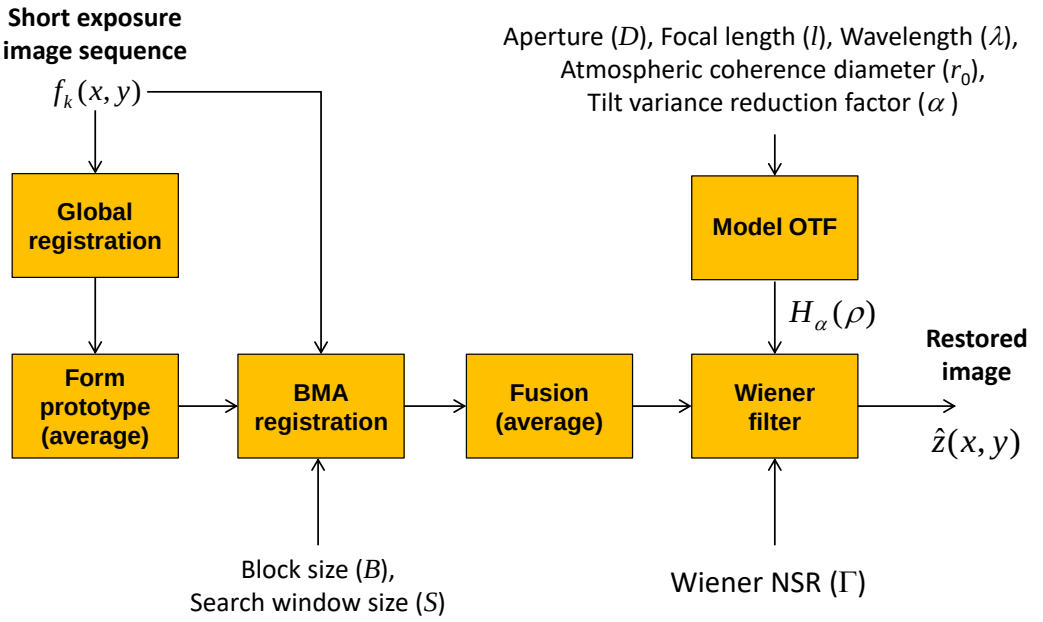

Figure 3. Proposed BMWF turbulence mitigation system block diagram.

3.2 BMWF turbulence mitigation

A block diagram representing the proposed BMWF turbulence mitigation algorithm is provided in Fig. 3.[3] The input is a set of N short-exposure frames $f_k(x,y)$, for $k = 1, 2, ..., N$. We shall assume that these frames are sampled such that they are free from aliasing. Treating turbulence and aliasing simultaneously has been explored,[17–20] but is beyond the scope of this paper.

The input frames are buffered and averaged. Next, robust global translational registration is used to align the N frames to the average. A least-squares gradient-based registration algorithm is used. This method is based on Lucas and Kanade,[21] but includes the robust multi-scale processing described by Hardie *et al.*[22,23] The frames are re-averaged after this global alignment, to produce the prototype image with the desired geometry. This step also gives us the opportunity to compensate for any camera platform motion. For ground based systems, translations may be sufficient. For airborne applications, affine registration at this stage may be appropriate.[22]

Next, a BMA algorithm[24] is used to estimate the motion local vectors for each pixel within each frame. The images are then interpolated, based on the motion vectors, so as to match the geometry of the prototype. As discussed in Section 3.1, the registration will not be ideal, and the accuracy of the registration is quantified by the parameter α (or β). Let us define the BMA block size as $B \times B$ pixels, and let the search window be $S \times S$ pixels in size (as defined by the position of the block centers). We use an exhaustive search within the search window, using the full rectangular blocks, and employ the mean absolute difference metric. We present results using a whole pixel search and subpixel search. The subpixel results are obtained by upsampling the images with bicubic interpolation.

The next step of the BMWF method is to simply average the registered frames, as shown in Fig. 3. This step is important for two main reasons. First, it reduces noise, and reduces the

impact of any BMA errors. Secondly, by averaging the spatially varying blurring, it allows us to accurately model the resulting blur as spatially invariant.[25] This justifies the use of a spatially invariant deconvolution step. The deconvolution step is implemented here using a parametric Wiener filter. The frequency response of the Wiener[26] filter is given by

$$H_W(u,v) = \frac{H_\alpha(u,v)^*}{|H_\alpha(u,v)|^2 + \Gamma}, \tag{8}$$

where Γ represents a constant noise-to-signal (NSR) power spectral density ratio. The output, after applying the Wiener filter, can be expressed as

$$\hat{z}(x,y) = FT^{-1}\left(H_W(u,v)F(u,v)\right), \tag{9}$$

where $F(u,v) = FT\{f(x,y)\}$, and $f(x,y)$ is the fused image in Fig. 3. Note that $FT(\cdot)$ and $FT^{-1}(\cdot)$ represent the Fourier and inverse Fourier transform, respectively. In practice, we are using sampled images and the fast Fourier transform (FFT) for implementing Eq. (9). Since we are assuming Nyquist sampled images, impulse invariance applies.[27] The images are padded symmetrically to minimize ringing artifacts associated with the circular convolution that results from FFT products.

Examples of the atmospheric OTF, $H_\alpha(\rho)$, are shown in Fig. 4 for $C_n^2 = 1.00 \times 10^{-15}$ m$^{-2/3}$ ($r_0 = 0.0478$ m). The optical system parameters corresponding to these plots are listed in Table 1. Also shown in Fig. 4 are the degradation OTFs multiplied by the Wiener filter transfer function in Eq. (8) for $\Gamma = 0.0002$ (the value used for the simulated and real data with 200 frames). Clearly, as α approaches 1 (equivalently β approaches 0), the degradation OTF is more favorable to high spatial frequencies. The signal will be above the noise floor out to a higher spatial frequency. Consequently, the Wiener filter is able to provide gain out to a higher spatial frequency, without being overwhelmed with noise. This greatly extends the effective restored system OTF. When the degradation OTF value gets below the noise floor, governed by Γ, the Wiener filter in Eq. (8) succumbs, as shown in Fig. 4. Note that with the illustrated NSR, the effective bandwidth of the sensor is nearly doubled going from the $\alpha = 0$ (no registration or tilt correction) to $\alpha = 1$ (full tilt correction). Matching the degradation model to the level of registration is essential in order to exploit the full benefits of the registration.

4. EXPERIMENTAL RESULTS

4.1 Simulation Validation

The experimental results presented have been generated using the optical parameters listed in Table 1, and simulation parameters in Table 2. Note that we are simulating a range of 7 km for a visible wavelength telescope and camera with a wavelength of $\lambda = 0.525$ μm. We have elected to use $N = 10$ phase screens (9 non-zero phase screens). The images are of size 257×257 pixels, and spatial sampling at the Nyquist frequency is used (based on the diffraction-limited optical cut-off frequency). We have generated sequences of $N = 200$ frames.

We have simulated a constant $C_n^2(z)$ profile with five levels of turbulence, ranging from $C_n^2 = 0.1 \times 10^{-15}$ m$^{-2/3}$ to $C_n^2 = 1.5 \times 10^{-15}$ m$^{-2/3}$. The ideal image and degraded image for

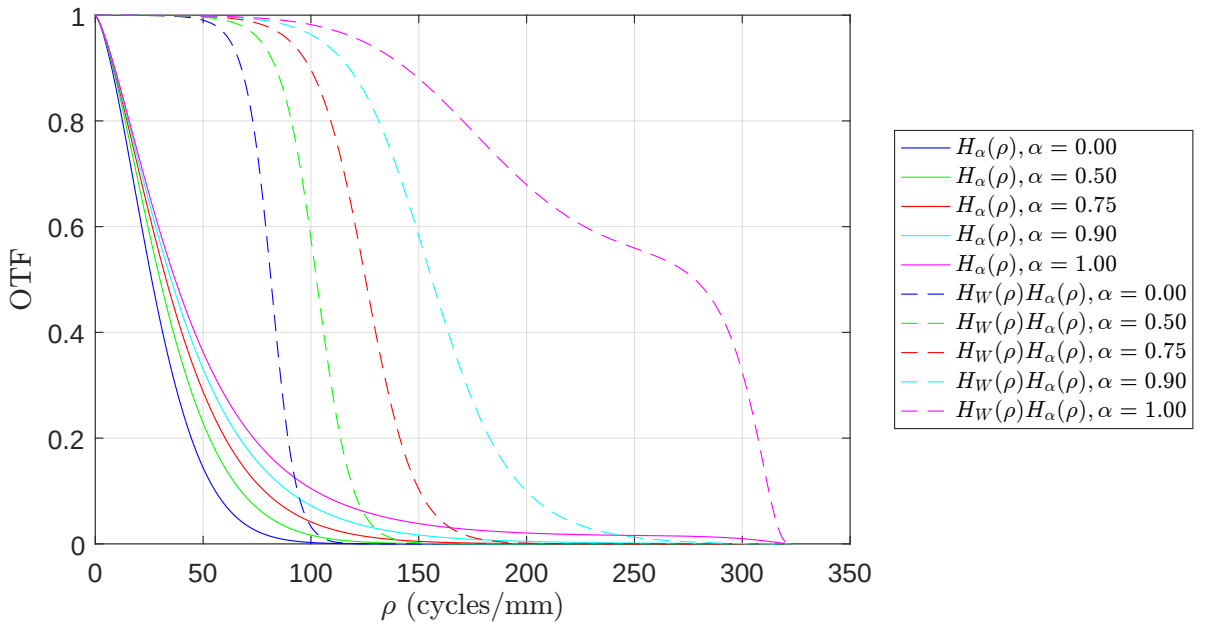

Figure 4. Overall system OTFs with different α for the optical system parameters in Table 1 with $C_n^2 = 1.00 \times 10^{-15}$ m$^{-2/3}$ ($r_0 = 0.0478$ m). The system OTFs multiplied by the Wiener filter frequency responses with $\Gamma = 0.0002$ are also shown to illustrate the effective OTF with restoration.

Table 1. Optical parameters.

Parameter	**Value**
Aperture	$D = 0.2034$ m
Focal length	$l = 1.2$ m
F-number	$f/\# = 5.9$
Wavelength	$\lambda = 0.525$ μm
Object distance	$L = 7$ km
Nyquist pixel spacing (focal plane)	$\delta_f = 1.5488$ μm
Nyquist pixel spacing (object plane)	$\delta_o = 9.0344$ mm

$C_n^2 = 1.00 \times 10^{-15}$ m$^{-2/3}$ are shown in Fig. 5. Also shown in Fig. 5(c) are the corresponding Z-tilt motion vectors, scaled by 2×.

Some of the validation results are presented in Table 3. The validation metrics listed are r_0, θ_0, and the root mean squared (RMS) Z-tilt. The Fried parameter is estimated from the simulation long-exposure PSF, obtained by averaging the generated PSFs over frames. The isoplanatic angle is estimated by an analysis of the wave function phases over the aperture for point sources of varying angular separations. Finally, the Z-tilt is estimated by performing a correlation based registration of the simulated PSFs. We have found that this type of correlation PSF registration corresponds well with Z-tilt, and PSF centroids correspond well to G-tilt. Note

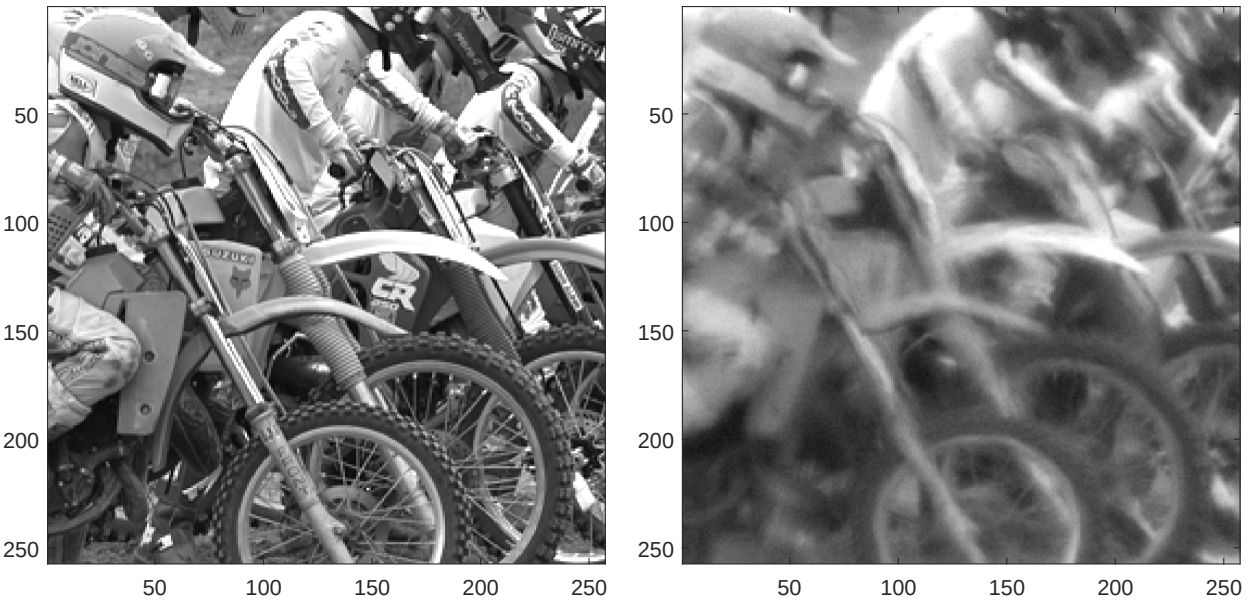

(a) (b)

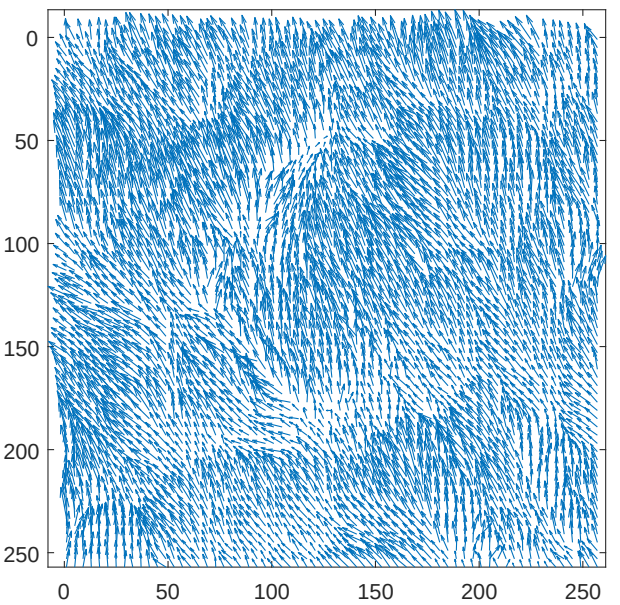

(c)

Figure 5. Simulated output images and tilt maps for constant C_n^2. (a) Ideal image, (b) output frame for $C_n^2 = 1.00 \times 10^{-15}$ m$^{-2/3}$; (c) tilt map for $C_n^2 = 1.00 \times 10^{-15}$ m$^{-2/3}$. Tilt vectors are scaled by 2×. All images are shown versus Nyquist pixel spacings.

Table 2. Simulation parameters

Parameter	**Value**
Path length	$L = 7$ km
Propagation step	$\Delta z = 700$ m
Cropped screen samples	$\mathcal{N} = 256$
Propagation screen width	$X = 0.9699$ m
Pupil plane point spread	$\tilde{D} = 0.8136$ m
Propagation sample spacing	$\Delta x = 0.0038$ m
Number of phase screens	$N = 10$ (9 non-zero)
Phase screen type	Modified von Kármán with subharmonics
Inner scale	$l_0 = 0.01$ m
Outer scale	$L_0 = 300$ m
Image size (pixels)	257×257 pixels
Image size (object plane)	2.3218×2.3218 m
Pixel skip	4 pixels (65×65 PSF array)

that we see a high level of agreement with regard to all of the metrics in Table 3.

Table 3. Constant C_n^2 simulation results. Comparison of theoretical statistical parameters and those estimated from the simulation output.

	$C_n^2 \times 10^{-15}$ ($\mathrm{m}^{-2/3}$)				
Parameter	0.10	0.25	0.50	1.00	1.50
Theoretical r_0 (m)	0.1901	0.1097	0.0724	0.0478	0.0374
Simulation r_0 (m)	0.1897	0.1111	0.0740	0.0491	0.0387
Percent Error	-0.21%	1.28%	2.21%	2.72%	3.48%
Theoretical θ_0 (μrads)	8.5401	4.9283	3.2515	2.1452	1.6819
Simulation θ_0 (μrads)	8.6071	5.1919	3.3938	2.1933	1.6928
Percent Error	0.78%	5.35%	4.38%	2.24%	0.65%
Theoretical θ_0 (pixels)	6.6170	3.8186	2.5193	1.6621	1.3032
Simulation θ_0 (pixels)	6.6689	4.0228	2.6296	1.6994	1.3116
Percent Error	0.78%	5.35%	4.38%	2.24%	0.64%
Theoretical RMS Z-tilt (pixels)	0.9026	1.4271	2.0182	2.8542	3.4957
Simulation RMS Z-tilt (pixels)	0.9044	1.4294	2.0151	2.8398	3.4692
Percent Error	0.20%	0.16%	-0.15%	-0.50%	-0.76%

The theoretical long and short exposure PSFs (with diffraction) are shown in Figs. 6 and 7, respectively. In particular, amplitude normalized cross-sections of the theoretical and simulated PSFs are shown for two turbulence levels. An excellent agreement can be seen here in all cases. Note that without subharmonics, the simulated long exposure PSFs tend to be too narrow, and the RMS Z-tilts tend to be too low. The relationship between these two parameters is explored

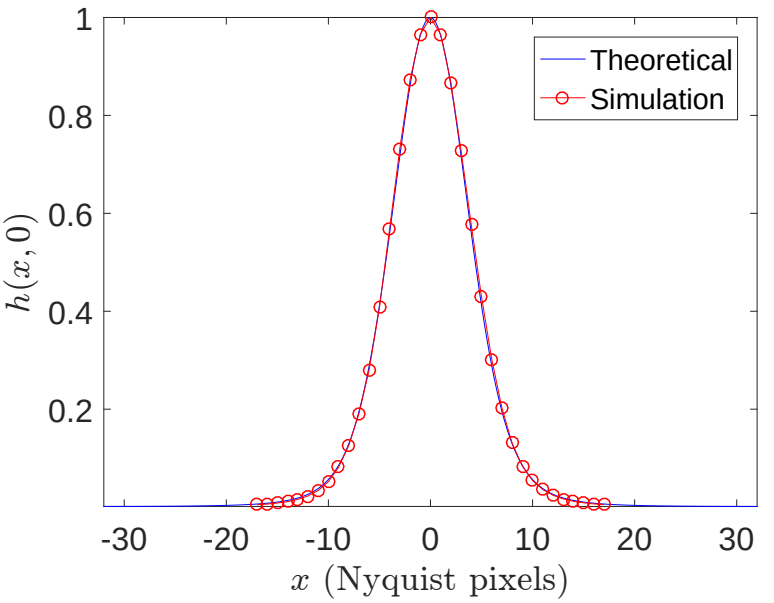

Figure 6. Comparison of theoretical and simulated long exposure PSFs for $C_n^2 = 1.00 \times 10^{-15}$ m$^{-2/3}$.

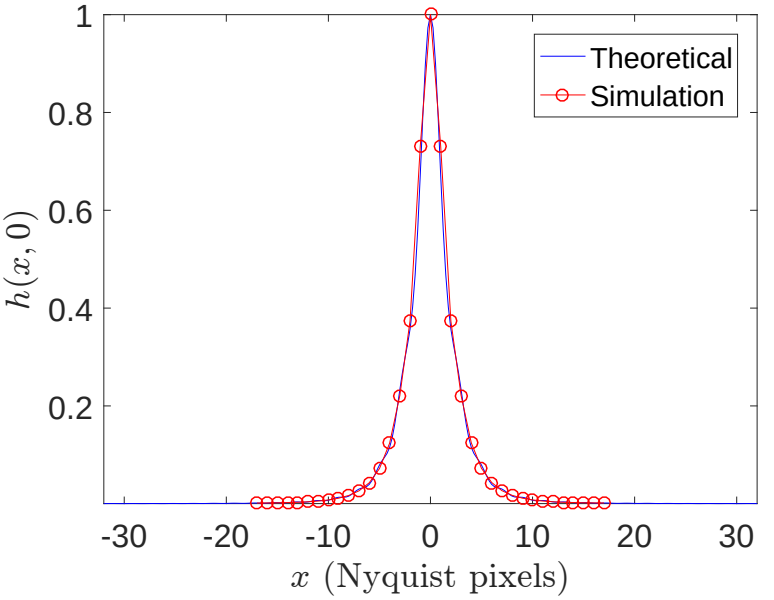

Figure 7. Comparison of theoretical and simulated short exposure (tilt corrected) PSFs for $C_n^2 = 1.00 \times 10^{-15}$ m$^{-2/3}$.

in depth by Hardie *et al.*[3]

Structure functions of phase[14] are shown in Figs. 8. These curves show the average squared phase difference over the aperture for two points separated by an angle of $\Delta\theta$. Note that the isoplanatic angle is defined to be the angle where these structure functions have a value of 1 radian. These plots show fairly good agreement between the theory and simulation. Thus, the

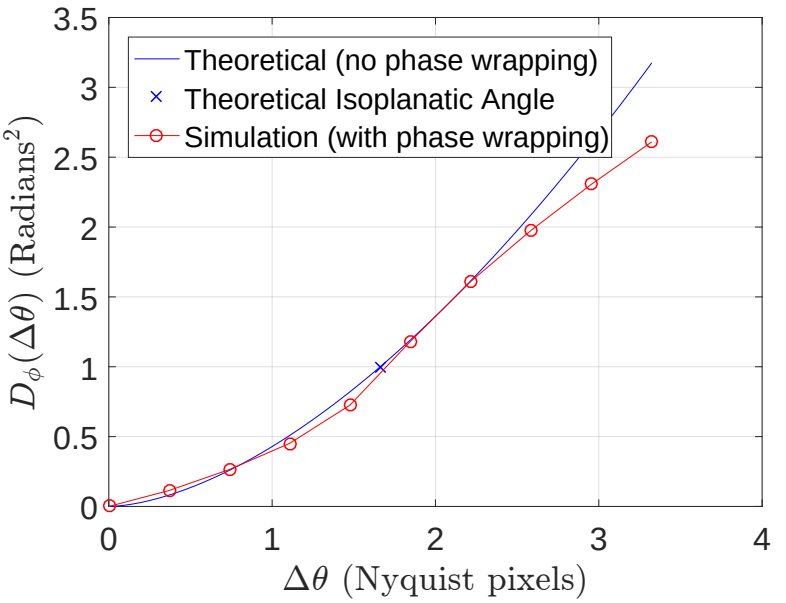

Figure 8. Comparison of theoretical and simulated structure functions of phase, revealing the isoplanatic angle where $D_\phi(\Delta\theta) = 1$ for $C_n^2 = 1.00 \times 10^{-15}$ m$^{-2/3}$.

simulation appears to be capable of accurately capturing small scale anisoplanatic behavior.

A comparison of theoretical and simulated Z-tilt correlations is shown in Fig. 9 for two turbulence levels. A similar comparison of the DTV is shown in Fig. 10. These curves show that the simulation is accurately producing the larger scale anisoplanatic behavior predicted by the theoretical expressions. Note that if a non-zero phase screen is placed at the pupil plane, we tend to see simulated correlation that is higher, and DTV that is lower, than the theoretical values. This is explained by the fact that all PSFs share the exact same phase screen at the pupil, because of the converging optical paths.

4.2 Turbulence Mitigation Results

4.2.1 Simulated data

The BMWF method is tested on five different levels of turbulence with $N = 200$ frames. Some statistical parameters for these scenarios are listed in Table 4. Additive independent Gaussian noise, with a standard deviation of $\sigma_\eta = 2$ digital units, is added to each simulated frame. The metric we use to evaluate the simulated data results is peak signal-to-noise-ratio (PSNR). The PSNR results are reported in Table 5.

The block size is a constant $B = 15$ pixels. We report results for both whole pixel BMA, and subpixel BMA in Table 5. We use the theoretical r_0 for each sequence for our OTF model. For the Wiener filter, we also report two sets of results. One where the optimum Γ and β are searched for and used, and another where fixed parameters are employed. The fixed NSR is $\Gamma = \sigma_\eta^2/(100N)$, where N is the number of frames. The fixed residual tilt factors are: $\beta = 1.0$ ($\alpha = 0.00$) for the Wiener filter applied to the raw frame average (i.e., long exposure PSF);

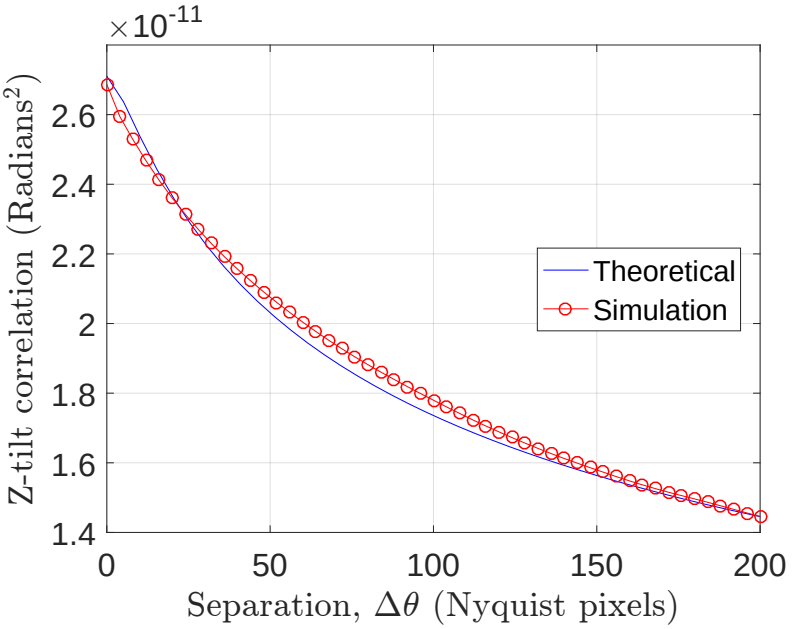

Figure 9. Comparison of theoretical and simulated Z-tilt correlations for $C_n^2 = 1.00 \times 10^{-15}$ m$^{-2/3}$. These are plotted versus versus $\Delta\theta$, which is expressed in terms of Nyquist pixel spacings here for the parameters in Table 1.

$\beta = 0.5$ ($\alpha = 0.75$) for the Wiener filter applied to the global registration average; and $\beta = 0.1$ ($\alpha = 0.99$) for the Wiener filter applied to BMA registered average. It is interesting to see in Table 5 how the PSNR increases by incorporating different levels of registration before averaging. As might be expected, the highest PSNR values are obtained with the BMA registration. It is also clear that there is a big boost in performance by adding the Wiener filter.

Table 4. Theoretical statistical parameters for the different levels of simulated atmospheric turbulence, and related restoration parameters.

	$C_n^2 \times 10^{15}$ (m$^{-2/3}$)				
Parameter	0.10	0.25	0.50	1.00	1.50
Isoplanatic angle θ_0 (Pixels)	6.62	3.82	2.52	1.66	1.30
BMA search size S (Pixels)	3.00	5.00	7.00	11.00	13.00
BMA block size B (Pixels)	15.00	15.00	15.00	15.00	15.00
Theoretical RMS G-tilt σ_r (Pixels)	0.8831	1.3962	1.9746	2.7925	3.4201
Estimated RMS G-tilt $\hat{\sigma}_r$ (Pixels)	0.8269	1.3781	1.9601	2.9022	3.5321
Theoretical $r_0(m)$	0.1902	0.1097	0.0724	0.0478	0.0375
Estimated $\hat{r}_0(m)$	0.2058	0.1115	0.0730	0.0456	0.0360

Let us now turn our attention to image results. The truth image is shown in Fig. 5(a). Several output images, formed using $N = 200$ and $C_n^2 = 1.00 \times 10^{-15}$ m$^{-2/3}$, are shown in Fig. 11. Figure 11(a) shows a single raw frame. Figure 11(b) shows the temporal frame average with

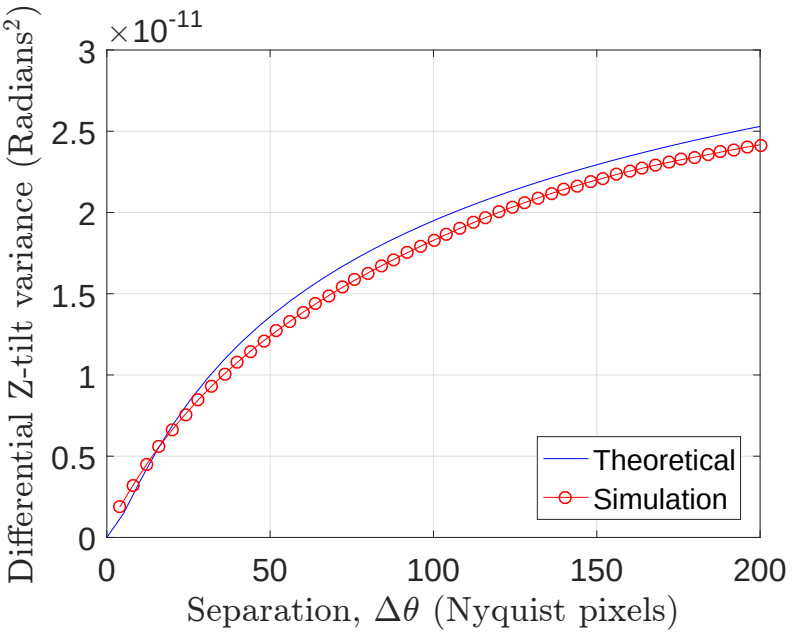

Figure 10. Comparison of theoretical and simulated differential Z-tilt variances for $C_n^2 = 1.00 \times 10^{-15}$ $\mathrm{m}^{-2/3}$. These are plotted versus versus $\Delta\theta$, which is expressed in terms of Nyquist pixel spacings here for the parameters in Table 1.

Table 5. PSNR (dB) results using 200 frames of simulated motorcycle image data with $\sigma_\eta = 2.0$.

	$C_n^2 \times 10^{15}$ $(\mathrm{m}^{-2/3})$				
Method	0.10	0.25	0.50	1.00	1.50
Raw frames	20.75	19.18	18.16	17.31	16.89
Average	21.77	20.24	19.10	18.07	17.54
Global reg. + average	22.63	21.24	19.99	18.78	18.14
BMA + average	23.11	22.09	20.88	19.48	18.71
BMA (sub) + average	23.19	22.15	20.93	19.51	18.73
Average + Wiener (optimized)	27.85	24.00	21.90	20.18	19.29
Average + Wiener ($\Gamma = 0.0002$, $\beta = 1.0$)	27.16	23.58	21.46	19.83	18.94
Global reg. + average + Wiener (optimized)	31.21	28.01	24.97	22.52	21.22
Global reg. + average + Wiener ($\Gamma = 0.0002$, $\beta = 0.5$)	30.96	27.92	24.96	22.51	21.22
BMA + average + Wiener (optimized)	31.27	30.03	28.65	26.00	23.66
BMA + average + Wiener ($\Gamma = 0.0002$, $\beta = 0.1$)	31.27	30.03	28.65	25.97	23.60
BMA (sub) + average + Wiener (optimized)	30.91	29.98	28.88	26.21	23.75
BMA (sub) + average + Wiener ($\Gamma = 0.0002$, $\beta = 0.1$)	30.91	29.98	28.84	26.13	23.67

no registration. The subpixel BMA registered frame average is shown in Fig. 11(c). Finally, the subpixel BMA + average + Wiener filter output is shown in Fig. 11(d). Here, the fixed parameter Wiener filter is used. Note that the temporal average in Fig. 11(b) is rather blurry, as it is effectively equivalent to the true image corrupted with the long-exposure PSF. The BMA

registered average has corrected geometry, and a blur level that is comparable to the observed short exposure frames. We see that by matching the PSF to the BMA registered average, excellent results are possible, as shown in Fig. 11(d).

4.2.2 Real data

Our final set of experimental results uses a real image sequence acquired from a tower to a truck and an engineering resolution target at a distance of 5 km. The resolution target is made up of a sequence of vertical and horizontal 3-line groups. The five large groups on the right side have bars with the following widths: 7.00 cm, 6.24 cm, 5.56 cm, 4.95 cm, and 4.91 cm. The optical parameters for this sensor are listed in Table 6. The sensor sampling is very close to Nyquist, so the Wiener filter is evaluated and implemented at the pixel pitch of the sensor (i.e., no resampling of the imagery is performed). A scintillometer is used to provide an estimate of r_0, as shown in Table 6. This value has been confirmed by analysis of an edge target, imaged within the larger field of view of the camera. Assuming a constant $C_n^2(z)$ profile, note that the isoplanatic angle, when converted to pixels, is only 0.25 pixels. This gives rise to warping that is highly uncorrelated at a small scale. This make BMA registration somewhat less effective than we saw in the simulated data. For this reason, we have selected to use a residual RMS tilt factor of $\beta = 0.4$ (compared with $\beta = 0.1$ for the simulated data).

The image results using the real data are shown in Fig. 12. Figure 12(a) shows raw frame 1. The 30 frame average + Wiener filter, using the long-exposure PSF with scintillometer r_0 is shown in Fig. 12(b). The subpixel BMA + average + Wiener output is shown for $N = 30$ and $N = 200$ in Figs. 12(c) and (d), respectively. Here we use $\beta = 0.4$, and $\Gamma = 0.0002$.

Table 6. Optical parameters for the real sensor data.

Parameter	**Value**
Aperture	$D = 57.150$ mm
Focal length	$l = 926$ mm
F-number	$f/\# = 16.203$
Wavelength	$\lambda = 0.785$ μm
Spatial cut-off freq.	$\rho_c = 78.620$ cyc/mm
Object distance	$L = 5$ km
Nyquist pixel spacing (focal plane)	$\delta_N = 6.36$ μm
Detector pitch (focal plane)	$\delta_s = 6.50$ μm
Undersampling	1.022
Scintillometer path averaged $C_n^2(z)$	$C_n^2 = 7.44 \times 10^{-15}$ m$^{-2/3}$
Isoplanatic angle (assuming constant $C_n^2(z)$)	$\theta_0 = 0.26$ (Pixels)
Scintillometer Fried parameter	$r_0 = 28.4$ mm
Estimated Fried parameter (for $\beta = 0.4$)	$\hat{r}_0 = 26.0$ mm
Theoretical RMS tilt for scintillometer r_0	$\sigma_r = 1.46$ (Pixels)
BMA Estimated RMS tilt (for $\beta = 0.4$)	$\hat{\sigma}_r = 1.61$ (Pixels)

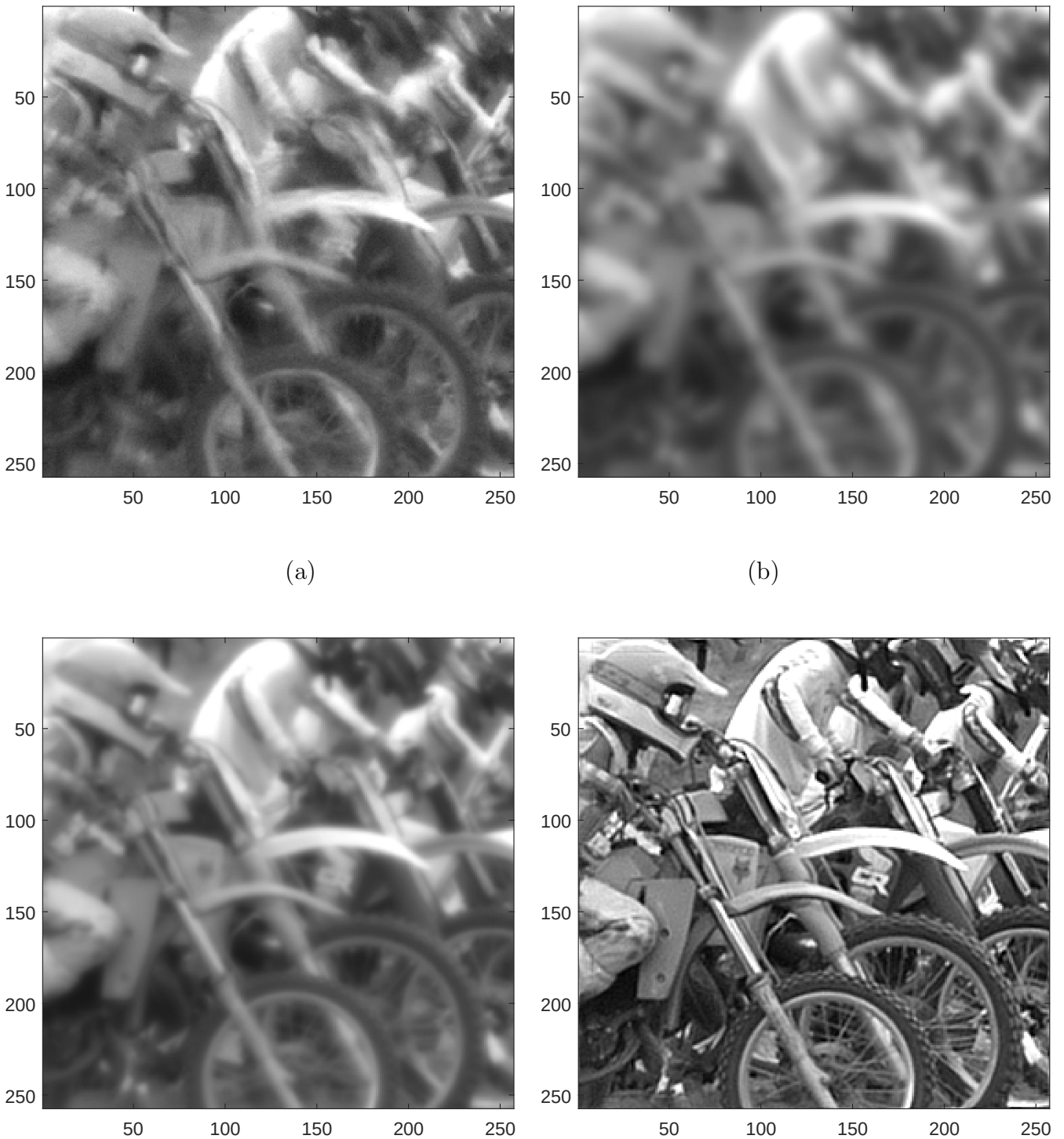

Figure 11. Restoration results using $N = 200$ frames with $C_n^2 = 1.00 \times 10^{-15}$ m$^{-2/3}$. (a) Raw frame 1; (b) raw frame average (no registration); (c) BMA registered frame average; (b) BMA (sub) +average + Wiener filter output.

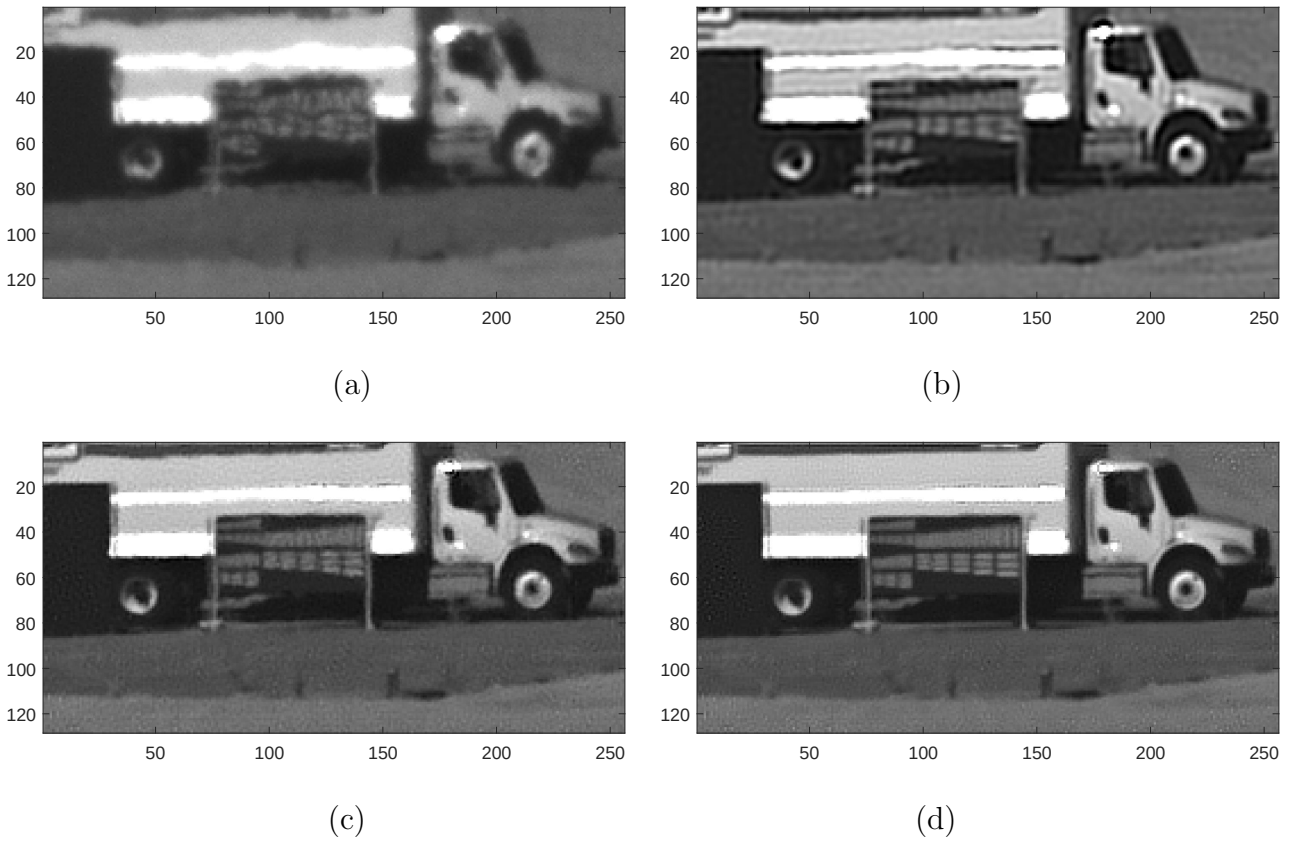

Figure 12. Restoration results using real image sequence. (a) First raw frame; (b) 30 frame average + Wiener filter output; (c) 30 frame BMA (sub) + average + Wiener filter output; (d) 200 frame BMA (sub) + average + Wiener filter output.

5. CONCLUSIONS

We have summarized key aspects of a new numerical wave propagation method for simulating imaging of an extended scene under anisoplanatic conditions.[2] In the simulation, we compute an array of PSFs for a 2D grid of points on the object plane. An ideal image is then degraded by applying the PSFs in a spatially varying weighted sum operation. This gives rise to a spatially varying blurring and warping degradation. The PSFs are generated by the propagation of point source through an array of phase screens. The optical path for each point is somewhat different, by virtue of its originating position on the object plane, and passes through different portions of the phase screens. This produces distinct, but spatially correlated PSFs.

Our novel validation analysis shows that this simulation is capable of generating accurate anisoplanatic effects on both a small and large scale. Small scale anisoplanaticism is validated with the isoplanatic angle. Large scale anisoplanaticism is validated for the first time using tilt correlation,[13] as well as with a newly derived DTV statistic for spherical waves.[2] We also find excellent agreement between the simulated and theoretical long- and short-exposure PSFs.

The BMWF restoration method utilizes a parametric OTF model for atmospheric turbulence and diffraction that incorporates the level of tilt correction provided by the registration step. We quantify the level of registration tilt correction by what we term the residual RMS tilt factor, β, or equivalently, the tilt variance reduction factor, $\alpha = 1 - \beta^2$. By matching the PSF model to the level of registration, improved results are possible.

ACKNOWLEDGMENTS

The authors would like to thank Michael Rucci and Matthew D. Howard at AFRL for performing the real data collection. This work has been supported in part by funding from L-3 Communications Cincinnati Electronics and under AFRL Award No. FA8650-10-2-7028 and FA9550-14-1-0244.

REFERENCES

[1] M. C. Roggemann and B. M. Welsh, *Imaging through Turbulence*, Laser and Optical Science and Technology, CRC Press (1996).

[2] R. C. Hardie, J. D. Power, D. A. LeMaster, D. R. Droege, S. Gladysz, and S. Bose-Pillai, "Simulation of anisoplanatic imaging through optical turbulence using numerical wave propagation with new validation analysis," *Optical Engineering* **56**(7), 071502 (2017).

[3] R. C. Hardie, M. A. Rucci, A. J. Dapore, and B. K. Karch, "Block matching and wiener filtering approach to optical turbulence mitigation and its application to simulated and real imagery with quantitative error analysis," *Optical Engineering* **56**(7), 071503 (2017).

[4] J. P. Bos and M. C. Roggemann, "Technique for simulating anisoplanatic image formation over long horizontal paths," *Optical Engineering* **51** (2012).

[5] C. J. Carrano, "Anisoplanatic performance of horizontal-path speckle imaging," *Proc. SPIE* **5162**, 14–27 (2003).

[6] R. W. Praus, K. Beardmore, and B. P. Venet, "The 'light tunneling' optical propagation method in wavetrain," *MZA Associates Corporation Technical Memorandum* (2007).

[7] J. P. Bos and M. C. Roggeman, "Simulation of extended scenes imaged through turbulence over horizontal paths," *Proc. SPIE* **8161**, 816106–816106–7 (2011).
[8] G. Monnier, F.-R. Duval, and S. Amram, "GPU-based simulation of optical propagation through turbulence for active and passive imaging," (2012).
[9] G. Monnier, F.-R. Duval, and S. Amram, "GPU-based simulation of optical propagation through turbulence for active and passive imaging," (2014).
[10] F. Dios, J. Recolons, A. Rodríguez, and O. Batet, "Temporal analysis of laser beam propagation in the atmosphere using computer-generated long phase screens," *Opt. Express* **16**, 2206–2220 (2008).
[11] J. P. Bos and M. C. Roggemann, "Mean squared error performance of speckle-imaging using the bispectrum in horizontal imaging applications," *Proc. SPIE* **8056**, 805603–805603–11 (2011).
[12] G. E. Archer, J. P. Bos, and M. C. Roggemann, "Comparison of bispectrum, multiframe blind deconvolution and hybrid bispectrum-multiframe blind deconvolution image reconstruction techniques for anisoplanatic, long horizontal-path imaging," *Optical Engineering* **53**(4), 043109 (2014).
[13] S. Basu, J. E. McCrae, and S. T. Fiorino, "Estimation of the path-averaged atmospheric refractive index structure constant from time-lapse imagery," *Proc. SPIE* **9465**, 94650T–94650T–9 (2015).
[14] J. D. Schmidt, *Numerical Simulation of Optical Wave Propagation with Examples in MATLAB*, SPIE Press Monograph, SPIE Press (2010).
[15] J. W. Goodman, *Introduction to Fourier Optics*, Roberts and Company Publishers, 3rd ed. (2004).
[16] M. Roggemann and B. Welsh, *Imaging through Turbulence*, CRC Press (1996).
[17] L. Yaroslavsky, B. Fishbain, G. Shabat, and I. Ideses, "Superresolution in turbulent videos: making profit from damage," *Opt. Lett.* **32**, 3038–3040 (2007).
[18] L. P. Yaroslavsky, G. Shabat, B. Fishbain, and I. A. Ideses, "Super-resolution of turbulent video: potentials and limitations," *Proc. SPIE* **6812**, 681205–681205–9 (2008).
[19] R. C. Hardie, D. R. Droege, B. S. Allen, A. J. Dapore, J. C. Blevins, and K. M. Hardin, "Real-time video processing for simultaneous atmospheric turbulence mitigation and super-resolution and its application to terrestrial and airborne infrared imaging," *Proceedings of the Military Sensing Symposia (MSS), Passive Sensors, Pasadena, CA* (2012).
[20] D. R. Droege, R. C. Hardie, B. S. Allen, A. J. Dapore, and J. C. Blevins, "A real-time atmospheric turbulence mitigation and super-resolution solution for infrared imaging systems," *Proc. SPIE* **8355**, 83550R–83550R–17 (2012).
[21] B. D. Lucas and T. Kanade, "An iterative image registration technique with an application to stereo vision," in *International Joint Conference on Artificial Intelligence, Vancouver*, (1981).
[22] R. C. Hardie, K. J. Barnard, and R. Ordonez, "Fast super-resolution with affine motion using an adaptive wiener filter and its application to airborne imaging," *Opt. Express* **19**, 26208–26231 (2011).
[23] R. C. Hardie and K. J. Barnard, "Fast super-resolution using an adaptive wiener filter with robustness to local motion," *Opt. Express* **20**, 21053–21073 (2012).
[24] Y.-W. Huang, C.-Y. Chen, C.-H. Tsai, C.-F. Shen, and L.-G. Chen, "Survey on block matching motion estimation algorithms and architectures with new results," *J. VLSI Signal Process. Syst.* **42**, 297–320 (2006).
[25] D. Fraser, G. Thorpe, and A. Lambert, "Atmospheric turbulence visualization with wide-area motion-blur restoration," *J. Opt. Soc. Am. A* **16**, 1751–1758 (1999).
[26] R. C. Gonzalez and R. E. Woods, *Digital Image Processing (3rd Edition)*, Prentice-Hall, Inc., Upper Saddle River, NJ, USA (2006).

[27] A. V. Oppenheim and R. W. Schafer, *Discrete-time Signal Processing (3rd Ed.)*, Prentice-Hall, Inc., Upper Saddle River, NJ, USA (2010).

Russell C. Hardie is a Full Professor in Department of Electrical and Computer Engineering at the University of Dayton, with a joint appointment in the Department of Electro-Optics and Photonics. Dr. Hardie received the University of Daytons top university-wide teaching award, the 2006 Alumni Award in Teaching. Dr. Hardie received the Rudolf Kingslake Medal and Prize from SPIE in 1998 for super-resolution research. In 1999, he received the School of Engineering Award of Excellence in Teaching, and the first annual Professor of the Year Award in 2002 from the student chapter of the IEEE.

Daniel LeMaster is the Technical Advisor for the EO Target Detection and Surveillance Branch in the Sensors Directorate of the Air Force Research Laboratory (AFRL). Dr. LeMaster has served as a conference chair, committee member, and guest journal editor for SPIE and has taught as an adjunct professor (Wright State University) and as a professional education instructor (Georgia Tech Research Institute). Prior to AFRL, he worked as a research engineer in the defense intelligence community and served in the U.S. Army.